IEEE Photonics Journal
An IEEE Photonics Society Publication

Open Access

A Single-Chip Integrated Spectrometer via Tunable Microring Resonator Array

Volume 11, Number 5, October 2019

Shaonan Zheng
Hong Cai
Junfeng Song
Jun Zou
Patricia Yang Liu
Zhiping Lin
Dim-Lee Kwong
Ai-Qun Liu

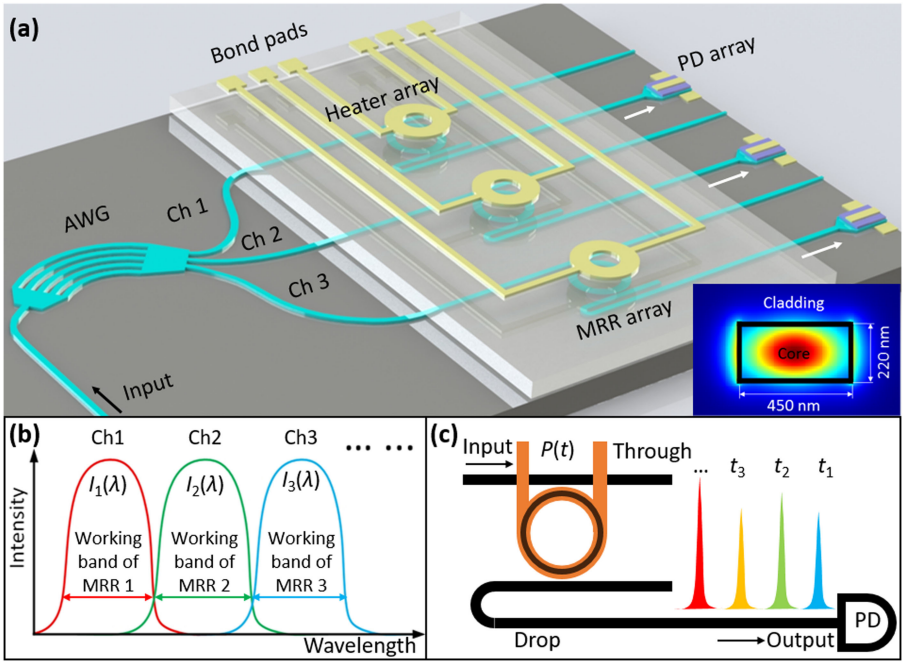

DOI: 10.1109/JPHOT.2019.2939580

A Single-Chip Integrated Spectrometer via Tunable Microring Resonator Array

Shaonan Zheng,[1,2] **Hong Cai**,[2] **Junfeng Song**,[3] **Jun Zou**,[1,4] **Patricia Yang Liu**,[1] **Zhiping Lin**,[1] **Dim-Lee Kwong**,[2] **and Ai-Qun Liu** [1]

[1]School of Electrical and Electronic Engineering, Nanyang Technological University, 639798 Singapore
[2]Institute of Microelectronics, A*STAR (Agency for Science, Technology and Research), 138634 Singapore
[3]College of Electronic Science and Engineering, Jilin University, Changchun 130012, China
[4]College of Science, Zhejiang University of Technology, Hangzhou 310023, China

DOI:10.1109/JPHOT.2019.2939580

Manuscript received July 31, 2019; revised August 29, 2019; accepted September 2, 2019. Date of publication September 5, 2019; date of current version September 19, 2019. This work was supported in part by Ministry of Education, Singapore under Tier 3 (MOE2017-T3-1-001) and Tier 1 (RG182/16 (S)) and in part by the Singapore National Research Foundation under the Competitive Research Program (NRF-CRP13-2014-01) and the Incentive for Research & Innovation Scheme (1102-IRIS-05-05) administered by EWI. Corresponding author: Ai-Qun Liu (e-mail: eaqliu@ntu.edu.sg).

Abstract: We experimentally demonstrate a spectrometer, which consists of an arrayed waveguide grating (AWG), tunable microring resonator (MRR) array, and waveguide-coupled Ge-on-Si photodetector, all integrated onto a single chip. The spectrometer achieves high resolution (0.1 ± 0.029 nm) and large bandwidth (25.4 nm) in 9 channels with a small footprint of 3×3 mm^2. It has high potential to enable a high-performance spectrometer for applications such as environmental monitoring, spectroscopy, biological and chemical sensing, etc.

Index Terms: Integrated optics, microring resonator, silicon photonics, sensing, spectroscopy, thermo-optic effect.

1. Introduction

On-chip spectrometer has critical impact on a wide range of applications such as environmental monitoring, spectroscopy, biological and chemical sensing, astronomy [1]–[7], etc. Leveraging the structures based on photonic integrated circuits (PIC) can dramatically reduce the size, weight and cost of spectroscopic instrumentations [8]–[14]. Besides, the availability of on-chip light sources and detectors promises a highly integrated and compact spectroscopic system [15]–[18]. There are mainly two approaches of on-chip spectrometers, i.e., Fourier transform (FT) spectrometer and dispersive spectrometer. On-chip FT spectrometer can deliver large bandwidth and high signal-to-noise ratio (SNR). FT spectrometer probing temporal interferogram requires only one detection channel, but it remains a challenge to achieve high resolution either due to limited optical path difference [19], [20] or under-sampling [21]. FT spectrometer detecting spatial interferogram [22]–[30] requires large number of detection channels to realize high resolution, degrading SNR. Hence, it is challenging to improve the resolution for the FT spectrometer. Other on-chip spectrometers reconstruct light by employing dispersive elements or tunable filters such as arrayed waveguide gratings (AWG) [5], [7], [8], [31]–[34], planar concave grating (PCG) [12], [34], [35], random structures [36]

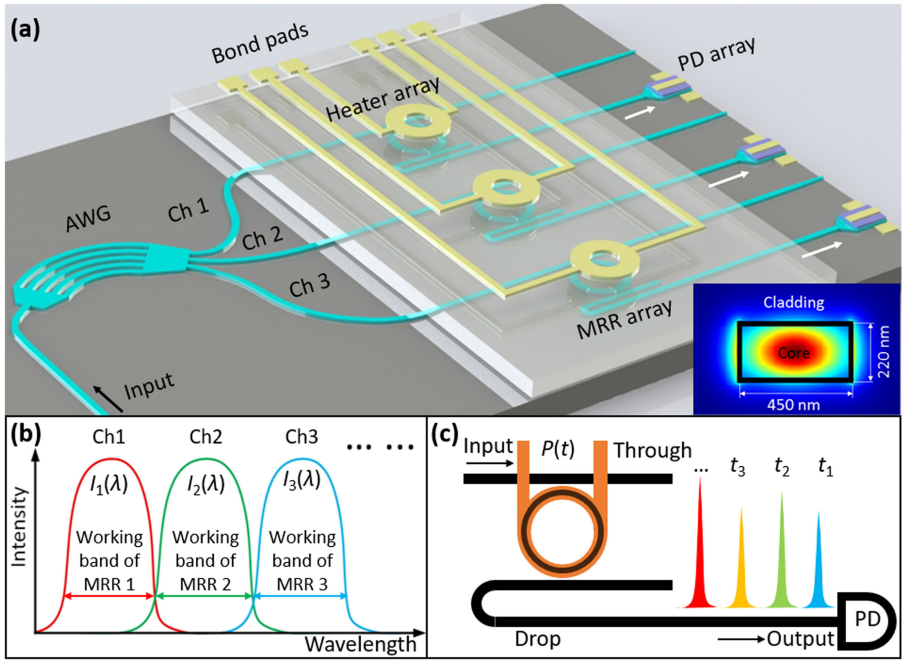

Fig. 1. (a) Schematic illustration of the spectrometer. The insert shows the cross section and modal profile of a single-mode waveguide. (b) The MRR working spectral band matches AWG transmission spectrum. (c) A thermally tunable MRR filter for spectrum reconstruction.

and photonic crystal [37]–[40]. However, there is inherent trade-off between resolution and channel count for dispersive spectrometers. As a result, large detection channel count is still required to achieve high resolution. For example, the spectrometer using stationary MRR array requires 84 channels to achieve a relatively high resolution (0.6 nm) and large bandwidth 56 nm [41]. Besides, it relies on e-beam lithography to realize radius control and fabricate MRRs with an ultra-small radius increment (1 nm).

In this paper, an integrated spectrometer is demonstrated using an AWG and tunable MRR array. The MRR can be thermally tuned with high resolution which depends only on the linewidth (sub-nanometer level) of the MRR resonance peak. By adopting MRR array, the bandwidth is largely extended to a maximal value equal to the free spectral range (FSR, up to 100 nm) of the AWG. Therefore, high resolution as well as large bandwidth are achieved, and the channel count is dramatically reduced. Integration of multiple spectrometer elements promises even larger bandwidth for environmental monitoring, spectroscopy, biological and chemical sensing, etc.

2. Design and Theoretical Analysis

The schematic spectrometer is shown in Fig. 1(a). It consists of an AWG, tunable MRR and waveguide-coupled Ge-on-Si photodetector. AWG is exploited to disperse the input broadband spectrum to a few separated spectral bands into corresponding channels. The tunable MRR in each channel reconstructs the corresponding dispersed spectrum with high resolution. By combining the reconstructed spectra from all channels, the full input spectrum can be retrieved.

The input spectrum $I_{in}(\lambda)$ is dispersed by AWG to separated spectral bands $I_1(\lambda)$, $I_2(\lambda)$, ..., $I_N(\lambda)$. The channel count of AWG, N is expressed as [42]

$$N = \frac{FSR}{\Delta\lambda_{ch}} \tag{1}$$

where FSR is free spectral range of AWG and $\Delta\lambda_{ch}$ is channel spacing. The dispersed spectral band into the MRR of Channel n is expressed as

$$I_n(\lambda) = f_n(\lambda) I_{in}(\lambda) \tag{2}$$

where n is an integer ($1 \leq n \leq N$) and $f_n(\lambda)$ is the envelope shaping the intensity of light into the MRR in Channel n. The tunable MRR in each channel functions as a high-resolution tunable filter to reconstruct the dispersed spectral bands. The working spectral band of an MRR denoted in Fig. 1(b) is defined as the tuning range of resonance wavelength from the initial value to the final value. The MRR working spectral bands should match the transmission spectra of the AWG such that the MRR working bandwidth equals to full width half maximum (FWHM) of transmission peak of the AWG (Fig. 1(b)). The working principle of a tunable MRR is shown in Fig. 1(c). When the MRR is thermally tuned, the resonance wavelength will be shifted to λ_r with respect to the initial value λ_0. The shift $\Delta\lambda$ is defined as $\lambda_r - \lambda_0$ and $\Delta\lambda$ is smaller than FSR of the MRR. Hence, when tuning the resonance wavelength in the time domain, each wavelength component in the input will be filtered and detected by the photodetector to obtain the temporal intensity $P(t)$. The tuning power $P(t)$ corresponds to the wavelength component λ in the reconstruction process.

The static temperature T of the MRR is proportional to the heating power P of titanium nitride (TiN) heater according to simulation results. Thus, temperature change ΔT can be written as $k_T P$, where k_T is heating efficiency. The refractive index of both Si and SiO_2 is wavelength and temperature dependent. The effective index n_{eff} of the quasi transverse electric (TE) mode of the waveguide depends on both the Si core and SiO_2 cladding. The effective index change is proportional to temperature excursion [20]. The resonance wavelength λ_r is proportional to Δn_{eff}, which is expressed as

$$\lambda_r = \lambda_0 + \frac{\lambda_0}{n_g} \Delta n_{eff} \tag{3}$$

where n_g is the group index. The output light detected by the photodetector $I_o(\lambda)$ in Channel n is expressed as $\mu_n(\lambda) f_n(\lambda) T_n(\lambda) I_{in}(\lambda)$. The coefficient $\mu_n(\lambda)$ is due to loss and dispersion during transmission, and $T_n(\lambda)$ is the transmission factor of the MRR in Channel n. The wavelength λ is within the working band of MRR in Channel n. As a result, the dispersed spectral band into Channel n, $I_{in}(\lambda)$ is expressed as

$$I_{in}(\lambda) = \frac{1}{\mu_n(\lambda) f_n(\lambda) T_n(\lambda)} I_o(\lambda) \tag{4}$$

The factor $1/(\mu_n(\lambda) f_n(\lambda) T_n(\lambda))$ can be obtained by proper calibration with a tunable laser source. Thus, the input spectrum $I_{in}(\lambda)$ within the working band of the MRR in Channel n is reconstructed by detecting the time-varying output light $I_o(\lambda)$. Since the same reconstruction processes apply to all channels, the full input spectrum $I_{in}(\lambda)$ can be retrieved by combining all the reconstructed spectra from all channels. The final resolution of the spectrometer depends on the resolution of the tunable MRR instead of the AWG channel spacing due to the ultra-narrow linewidth ($\sim$0.076 nm here) of the MRR resonance peak. Each tunable MRR works within a certain bandwidth BW. Hence, by using paralleled tunable MRR array (N), the working bandwidth is extended to $N \times$ BW.

3. Experimental Results and Discussion

The spectrometer is fabricated using silicon on insulator wafer (220 nm top Si layer) by the nano-silicon-photonic fabrication processes. The 248 nm deep ultraviolet optical lithography is used. The waveguide is firstly formed by partially etching the top Si layer. Thereafter, implantation processes with Boron into the Si substrate and contact area of photodetector are performed. Then, the Ge window is open to expose the Si substrate of photodetector and Ge is selectively grown on Si through epitaxy processes. Phosphorus is implanted into the top surface of Ge to form p-i-n type waveguide-coupled Ge-on-Si photodetector. Subsequently, an upper SiO_2 cladding layer is deposited through plasma-enhanced chemical vapor deposition process for passivation. Then TiN is formed as a

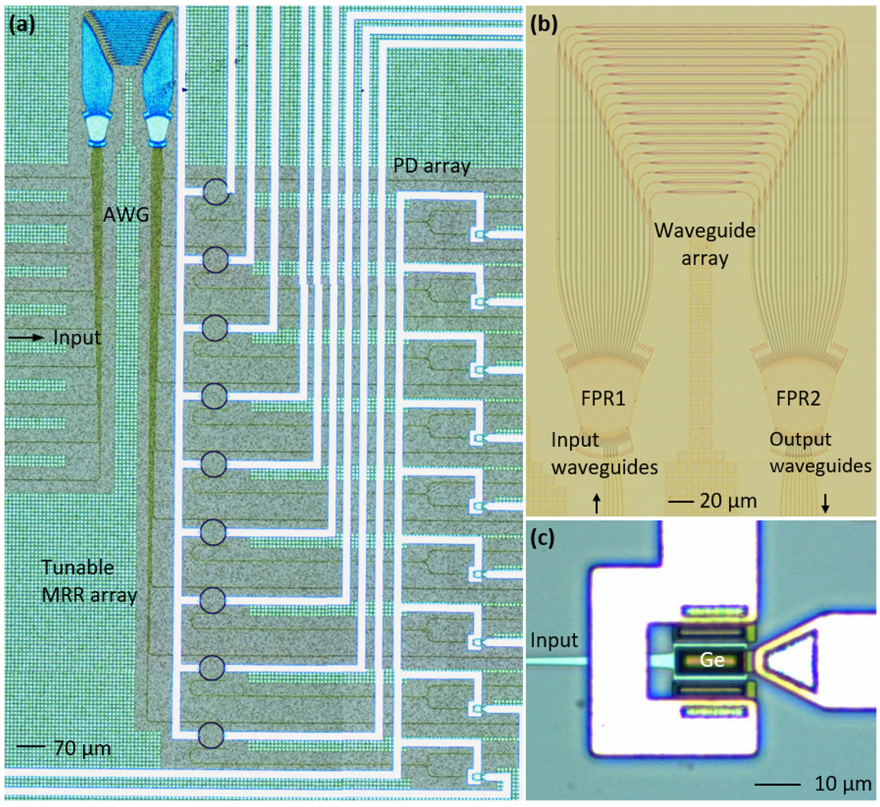

Fig. 2. Optical micrographs of (a) the fabricated spectrometer, (b) a fabricated AWG, and (c) a waveguide-coupled Ge-on-Si photodetector.

resistive layer for heaters. An aluminum thin film is then patterned as electrical connection to power heaters and photodetectors.

The optical micrograph of the spectrometer is shown in Fig. 2(a). There are 9 MRRs, namely 9 spectral channels. In each channel, a tunable MRR is cascaded with each output waveguide of the AWG and the drop port of the MRR is connected to a waveguide-coupled Ge-on-Si photodetector. Fig. 2(b) shows the optical micrograph of a fabricated AWG, which consists of input and output waveguide array, and free propagation region (FPR) in the input and output region. It has 5 input waveguides, 19 waveguides in the waveguide array and 9 output waveguides. The input waveguide aligning with the center of FPR 1 is the input port, while the other 4 input waveguides are designed as backups for different central wavelengths. Rib waveguide is designed for the waveguide array to reduce optical loss and phase error due to fabrication variation. Fig. 2(c) shows the optical micrograph of a waveguide-coupled Ge-on-Si photodetector. The time-varying electric signals from the photodetectors are read out by a laptop via a microcontroller.

The rib width of the waveguide is designed as 800 nm, the rib thickness is 220 nm and the slab thickness is 90 nm. The transmission spectra from 9 output channels of the AWG with a broadband source (Amonics ALS-CL-13B-FA) input are shown in Fig. 3(a). The source spectrum is subtracted for normalization. The measured FSR of the AWG is 27 nm. The channel spacing is 3.306 nm. The FWHM is 2.312 nm and the crosstalk range is 13.62–16.20 dB. Fig. 3(b) shows that the resonance wavelength of the MRR in Channel 3 is red-shifted while sweeping heating power on the heater. The resonance wavelength is well fitted to heating power with a linear equation. Fig. 3(c) shows the normalized detected intensity by the photodetector with a tunable laser source (Santec TSL-550, TLS-1) input in Channel 3. Different colors indicate different input wavelengths. TLS-1 is set at one wavelength and then the photodetector detects the time-varying intensity while

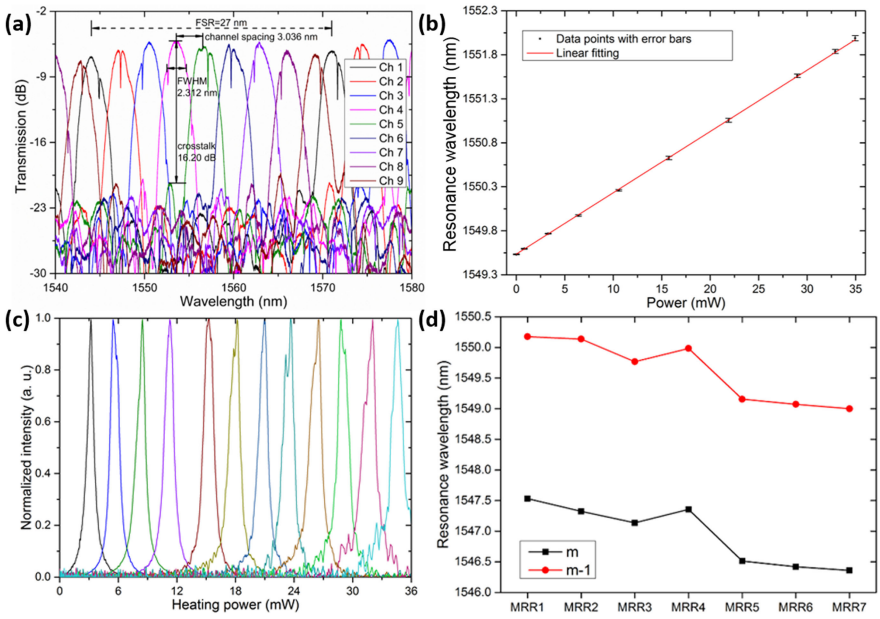

Fig. 3. (a) Transmission spectra from 9 output channels. (b) Relation between resonance wavelength and applied electric power on the heater in Channel 3. The error bar denotes standard deviation. (c) Detected power by photodetector while sweeping applied heating power on the heater in Channel 3. (d) Resonance wavelength variation of 7 identical MRRs by design due to fabrication variation.

sweeping the heating power. Thereafter, TLS-1 is set at another wavelength for detection. The wavelength increment is 0.2 nm. The detected peaks correspond to input wavelengths. The non-constant wavelength spacing is due to temperature variation. Hence, the wavelength of the input spectrum can be retrieved by heating power and the intensity can be retrieved by corresponding detected peak power by photodetector. The designed average radius of the MRR is 33.9 μm. The cross section is 450 $\times$ 220 nm^2. The experimentally measured FSR of the MRR is 2.676 nm at 1555.496 nm. The linewidth is 0.076 nm at 1571.668 nm with quality factor $\sim$2 $\times$10^4. The tuning efficiency is 0.07 nm/mW.

Seven identical MRRs are fabricated and measured when no heating power is applied. The maximal resonance wavelength variation is 1.2 nm as shown in Fig. 3(d). It means that due to fabrication variation, the resonance wavelength cannot be precisely controlled by simply changing the dimensions of the MRR. The tunable MRR adopted here can actively control the resonance wavelength well.

For characterization of the spectrometer, TLS-1 is used. The normalized retrieved spectra from the 9 channels with TLS-1 input are shown in Fig. 4(a). The wavelength increment is 0.2 nm. The normalized retrieved spectra from Channel 8 with TLS-1 input are shown in Fig. 4(b). The wavelength increment is 0.1 nm. The working spectral ranges of the 9 channels add up to a total bandwidth of 25.4 nm. For resolution characterization of the spectrometer, TLS-1 and another tunable laser source (ANDO AQ4321D, TLS-2) are input simultaneously [21], [22]. The normalized retrieved spectra from Channel 8 are shown in Fig. 4(c). TLS-1 and TLS-2 are set at different wavelengths, i.e., 1566 and 1566.1 nm, 1566 and 1567 nm, respectively. The two wavelength components with 0.1 nm separation are differentiated. Hence, the spectrometer achieves a high resolution of 0.1 nm with a large bandwidth of 25.4 nm.

The spectrometer achieves 0.1 nm resolution and 25.4 nm bandwidth (within one FSR) with only 9 channels. The number of resolved channels (defined as the available bandwidth/minimum linewidth) is 25.4/0.1 $=$ 254. Therefore, compared to approach either using static MRRs [41] or using an AWG [5], [7], [8], [31]–[34], both requiring large channel count achieve high resolving power, it is more compact (3 $\times$ 3 mm^2) and the 9 channels produces higher throughput, thereby

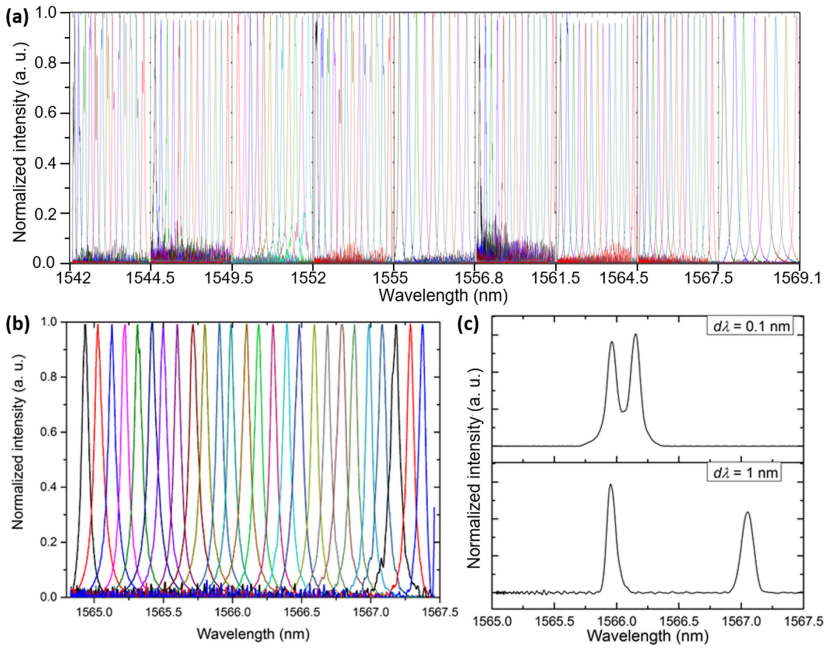

Fig. 4. (a) Normalized retrieved spectra from the 9 channels with TLS-1 (set at 0.2 nm wavelength increment) input. (b) Normalized retrieved spectra from Channel 8 with TLS-1 (set at 0.1 nm wavelength increment) input. (c) Normalized retrieved spectra from Channel 8 with TLS-1 and TLS-2 input simultaneously with 0.1 nm and 1 nm wavelength separation, respectively.

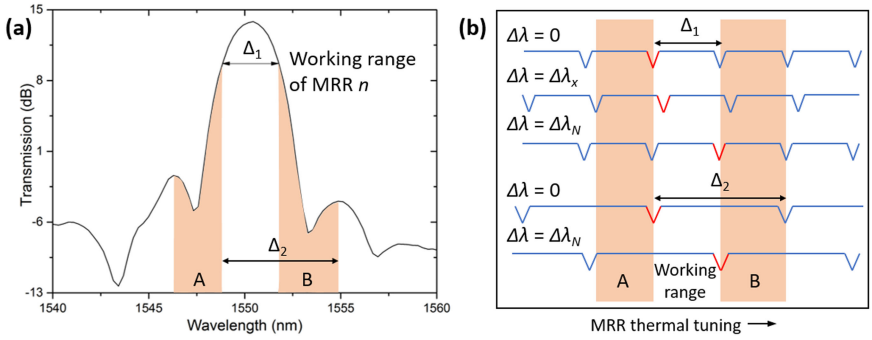

Fig. 5. (a) AWG crosstalk range in channel *n*. Δ_1 equals to bandwidth of MRR working range. Δ_2 equals to bandwidth of working range plus half of crosstalk range. (b) Resonance wavelength tuning at two different FSR values, i.e., Δ_1 and Δ_2.

higher SNR. High quality factor (*Q*) value of MRR enables ultra-fine resonance wavelength tuning. The resolution can be further improved by increasing the *Q* value of MRR through coupler design and fabrication optimization. The bandwidth of a single spectrometer element equals to the FSR of the AWG, which can be as large as 100 nm. The total bandwidth can be dramatically extended through a paralleled spectrometer element array. The AWG channel crosstalk will affect the SNR. For example, the crosstalk ranges in Channel n are denoted by A and B as shown in Fig. 5(a). The working resonance position denoted in red is tuned from 0 to $\Delta\lambda_N$ as shown in Fig. 5(b). Firstly, the condition is considered when the free spectral range of the MRR equals to the bandwidth of MRR working range, i.e., FSR $= \Delta_1$. When the MRR is tuned to $\Delta\lambda_x$, the resonance position on the left of the working position enters crosstalk range A and the resonance position on the right enters

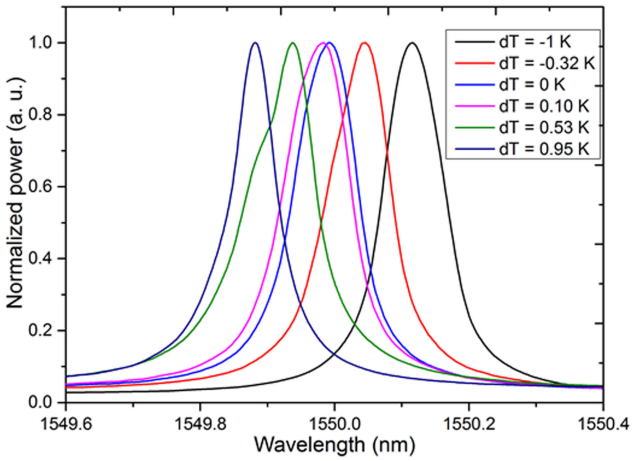

Fig. 6. Retrieved spectra with TLS-1 (set at 1550 nm) input at different temperature detuning values.

range B. When MRR tuning from $\Delta\lambda_x$ to $\Delta\lambda_N$, the two positions will add noise to the detected power by photodetector. This noise level is increased with decreasing crosstalk value, which leads to low SNR and small dynamic range. However, when FSR $= \Delta_2$, only the working resonance position exists in the working range and the two crosstalk ranges during MRR tuning. It means that when FSR $> \Delta_2$, the influence of crosstalk on SNR is mitigated. Therefore, SNR will be increased with larger crosstalk value and/or optimized FSR of MRR. The experimentally detected FWHM of AWG (2.312 nm) is smaller than the FSR of the MRR ($\sim$2.676 nm). Based on testing result, the maximum value of Δ_2 is 5.836 nm. To increase SNR and dynamic range, the FSR of the MRR can be designed to be larger than 5.836 nm. The insertion loss of the AWG is 5.18 dB, including 3 dB fibre-chip coupling loss and 2.18 dB on-chip loss. The insertion loss of the spectrometer from the input fiber to the photodiode is $\sim$8.77 dB. The insertion loss can be reduced by reducing transmission loss via fabrication improvement and/or reducing the optical loss in AWG [43] to increase SNR and dynamic range. The power error origins from fiber vibration, and the wavelength error origins from temperature variation. Fiber vibration will not present when the fiber is permanently fixed to the chip.

Temperature variation will affect the resonance positions of the MRRs as can be seen from. As shown in Fig. 6, wavelength is detuned due to temperature variation, which will affect the wavelength accuracy. A Peltier plate connected to a thermoelectric controller under the spectrometer chip is exploited to stabilize the temperature.

4. Conclusion

In conclusion, a tunable microring resonator array-based spectrometer is experimentally demonstrated, which is integrated with the arrayed waveguide grating and waveguide-coupled Ge-on-Si photodetector array onto a single chip. The spectrometer overcomes the trade-off between resolution and channel count in existing on-chip spectrometers to realize high resolution with a few channels. The thermally tunable MRR in each channel works as a high-resolution filter to reconstruct the dispersed spectrum by the time-varying light intensity detected by the corresponding photodetector. By combining all the reconstructed spectra from all channels, the original spectrum can be retrieved. It achieves a high resolution of 0.1 nm and a large bandwidth of 25.4 nm in 9 channels with a compact size of 3 $\times$ 3 mm^2. The bandwidth will be significantly increased when using paralleled spectrometer element array. It is promising to be applied in environmental monitoring, spectroscopy, and biological and chemical sensing.

References

[1] J. Antila *et al.*, "MEMS-and MOEMS-based near-infrared spectrometers," in *Encyclopedia Analytical Chemistry*, U.S.: Wiley, 2014, pp. 1–36.

[2] D. Sorak, L. Herberholz, S. Iwascek, S. Altinpinar, F. Pfeifer, and H. W. Siesler, "New developments and applications of handheld Raman, mid-infrared, and near-infrared spectrometers," *Appl. Spectrosc. Rev.*, vol. 47, no. 2, pp. 83–115, 2012.

[3] R. E. Myers, "Handheld laser-induced breakdown spectroscopy instruments and their applications," in *Encyclopedia Analytical Chemistry: Applications, Theory Instrumentation*, Wiley, 2006, pp. 1–8.

[4] R. Wolffenbuttel, "MEMS-based optical mini- and microspectrometers for the visible and infrared spectral range," *J. Micromechanics Microengineering*, vol. 15, no. 7, p. S145–S152, 2005.

[5] P. Gatkine, S. Veilleux, Y. Hu, J. Bland-Hawthorn, and M. Dagenais, "Towards a multi-input astrophotonic AWG spectrograph," in *Proc. Soc. Photo-Opt. Instrum. Engineers- Int. Soc. Opt. Eng.*, Advances in Optical and Mechanical Technologies for Telescopes and Instrumentation III, vol. 10706, Austin, TX, USA, 2018, p. 1070656.

[6] J. Bland-Hawthorn and G. Leon-Saval, "Astrophotonics: molding the flow of light in astronomical instruments [Invited]," *Opt. Exp.*, vol. 25, no. 13, pp. 15549–15557, 2017.

[7] P. Gatkine, S. Veilleux, Y. Hu, J. Bland-Hawthorn, and M. Dagenais, "Arrayed waveguide grating spectrometers for astronomical applications: new results," *Opt. Exp.*, vol. 25, no. 15, pp. 17918–17935, 2017.

[8] E. Ryckeboer, X. Nie, A. Dhakal, D. Martens, P. Bienstman, G. Roelkens, and R. Baets, "Spectroscopic sensing and applications in silicon photonics," in *Proc. IEEE 14th Int. Conf. Group IV Photon.*, 2017, pp. 81–82.

[9] A. Dhakal, AZ. Subramanian, P. Wuytens, F. Peyskens, N. Le Thomas, and R. Baets, "Evanescent excitation and collection of spontaneous Raman spectra using silicon nitride nanophotonic waveguides," *Opt. Lett.*, vol. 39, no. 13, pp. 4025–4028, 2014.

[10] E. Ryckeboer, R. Bockstaele, M. Vanslembrouck, and R. Baets, "Glucose sensing by waveguide-based absorption spectroscopy on a silicon chip," *Biomedical Opt. Exp.*, vol. 5, no. 5, pp. 1636–1648, 2014.

[11] L. Tombez, E. Zhang, J. Orcutt, S. Kamlapurkar, and W. Green, "Methane absorption spectroscopy on a silicon photonic chip," *Optica*, vol. 4, no. 11, pp. 1322–1325, 2017.

[12] E. Ryckeboer *et al.*, "Silicon-on-insulator spectrometers with integrated GaInAsSb photodiodes for wide-band spectroscopy from 1510 to 2300 nm," *Opt. Exp.*, vol. 21, no. 5, pp. 6101–6108, 2013.

[13] H. Lin *et al.*, "Mid-infrared integrated photonics on silicon: A perspective," *Nanophotonics*, vol. 7, no. 2, pp. 393–420, 2017.

[14] A. Z. Subramanian *et al.*, "Silicon and silicon nitride photonic circuits for spectroscopic sensing on-a-chip [Invited]," *Photon. Res.*, vol. 3, no. 5, pp. B47–B59, 2015.

[15] R. Wang *et al.*, "III–V-on-silicon photonic integrated circuits for spectroscopic sensing in the 2–4 μm wavelength range," *Sensors*, vol. 17, no. 8, p. 1788, 2017.

[16] Z. Zhou, B. Yin, and J. Michel, "On-chip light sources for silicon photonics," *Light: Sci. Appl.*, vol. 4, no. 11, p. e358, 2015.

[17] J. Michel, J. Liu, and L. C. Kimerling, "High-performance Ge-on-Si photodetectors," *Nature Photon.*, vol. 4, no. 8, pp. 527–534, 2010.

[18] K.-W. Ang, G.-Q. Lo, and D.-L. Kwong, "Germanium photodetector technologies for optical communication applications," in *Semiconductor Technologies*, InTech, 2010, pp. 373–406.

[19] S. Zheng, H. Cai, Y. D. Gu, L. K. Chin, and A. Q. Liu, "On-chip fourier transform spectrometer for chemical sensing applications," in *Proc. Conf. Lasers Electro-Opt.*, San Jose, CA, USA, 2016, p. AM1J.6.

[20] M. C. Souza, A. Grieco, N. C. Frateschi, and Y. Fainman, "Fourier transform spectrometer on silicon with thermo-optic non-linearity and dispersion correction," *Nature Commun.*, vol. 9, no. 1, 2018, Art. no. 665.

[21] D. M. Kita *et al.*, "High-performance and scalable on-chip digital Fourier transform spectroscopy," *Nature Commun.*, vol. 9, no. 1, 2018, Art. no. 4405.

[22] M. Florjańczyk, P. Cheben, S. Janz, A. Scott, B. Solheim, and D. X. Xu, "Multiaperture planar waveguide spectrometer formed by arrayed Mach-Zehnder interferometers," *Opt. Exp.*, vol. 15, no. 26, pp. 18176–18189, 2007.

[23] M. Florjańczyk *et al.*, "Development of a slab waveguide spatial heterodyne spectrometer for remote sensing," in *Proc. Soc. Photo-Opt. Instrum. Engineers-Int. Soc. Opt. Eng.*, MOEMS Miniaturized Syst. IX, vol. 7594, 2010, p. 75940R.

[24] P. J. Bock *et al.*, "Subwavelength grating Fourier-transform interferometer array in silicon-on-insulator," *Laser Photon. Rev.*, vol. 7, no. 6, pp. L67–L70, 2013.

[25] A. V. Velasco *et al.*, "High-resolution Fourier-transform spectrometer chip with microphotonic silicon spiral waveguides," *Opt. Lett.*, vol. 38, no. 5, pp. 706–708, 2013.

[26] H. Podmore *et al.*, "Demonstration of a compressive-sensing Fourier-transform on-chip spectrometer," *Opt. Lett.*, vol. 42, no. 7, pp. 1440–1443, 2017.

[27] E. Le Coarer *et al.*, "Wavelength-scale stationary-wave integrated Fourier-transform spectrometry," *Nature Photon.*, vol. 1, no. 8, pp. 473–478, 2007.

[28] G. D. Osowiecki *et al.*, "Standing wave integrated Fourier transform spectrometer for imaging spectrometry in the near infrared," in *Proc. Soc. Photo-Opt. Instrum. Engineers Opt. Eng.+ Appl., Int. Soc. Opt. Eng.*, vol. 9611, 2015, p. 96110P.

[29] M. Madi, F. Ceyssens, I. Shorubalko, H. P. Herzig, B. Guldimann, and P. Giaccari, "Lippmann waveguide spectrometer with enhanced throughput and bandwidth for space and commercial applications," *Opt. Exp.*, vol. 26, no. 3, pp. 2682–2707, 2018.

[30] X. Nie, E. Ryckeboer, G. Roelkens, and R. Baets, "CMOS-compatible broadband co-propagative stationary Fourier transform spectrometer integrated on a silicon nitride photonics platform," *Opt. Exp.*, vol. 25, no. 8, pp. A409–A418, 2017.

[31] P. Cheben *et al.*, "A 100-channel near-infrared SOI waveguide microspectrometer: Design and fabrication challenges," in *Proc. Soc. Photo-Opt. Instrum. Engineers-Int. Soc. Opt. Eng.*, Optoelectronic Devices Integration, vol. 5644, 2005, pp. 103–110.
[32] P. Cheben *et al.*, "A high-resolution silicon-on-insulator arrayed waveguide grating microspectrometer with sub-micrometer aperture waveguides," *Opt. Exp.*, vol. 15, no. 5, pp. 2299–2306, 2007.
[33] N. Cvetojevic, N. Jovanovic, J. Lawrence, M. Withford, and J. Bland-Hawthorn, "Developing arrayed waveguide grating spectrographs for multi-object astronomical spectroscopy," *Opt. Exp.*, vol. 20, no. 3, pp. 2062–2072, 2012.
[34] M. Muneeb *et al.*, "Demonstration of silicon-on-insulator mid-infrared spectrometers operating at 3.8 μm," *Opt. Exp.*, vol. 21, no. 10, pp. 11659–11669, 2013.
[35] B. B. Kyotoku, L. Chen, and M. Lipson, "Sub-nm resolution cavity enhanced micro-spectrometer," *Opt. Exp.*, vol. 18, no. 1, pp. 102–107, 2010.
[36] B. Redding, S. F. Liew, R. Sarma, and H. Cao, "Compact spectrometer based on a disordered photonic chip," *Nature Photon.*, vol. 7, no. 9, pp. 746–751, 2013.
[37] B. Momeni, E. S. Hosseini, and A. Adibi, "Planar photonic crystal microspectrometers in silicon-nitride for the visible range," *Opt. Exp.*, vol. 17, no. 19, pp. 17060–17069, 2009.
[38] B. Momeni, E. S. Hosseini, M. Askari, M. Soltani, and A. Adibi, "Integrated photonic crystal spectrometers for sensing applications," *Optics Commun.*, vol. 282, no. 15, pp. 3168–3171, 2009.
[39] Ž. Zobenica *et al.*, "Integrated nano-opto-electro-mechanical sensor for spectrometry and nanometrology," *Nature Commun.*, vol. 8, no. 1, 2017, Art. no. 2216.
[40] A. C. Liapis, B. Gao, M. R. Siddiqui, Z. Shi, and R. W. Boyd, "On-chip spectroscopy with thermally tuned high-Q photonic crystal cavities," *Appl. Phys. Lett.*, vol. 108, no. 2, 2016, Art. no. 021105.
[41] Z. Xia *et al.*, "High resolution on-chip spectroscopy based on miniaturized microdonut resonators," *Opt. Exp.*, vol. 19, no. 13, pp. 12356–12364, 2011.
[42] M. K. Smit and C. Van Dam, "PHASAR-based WDM-devices: Principles, design and applications," *IEEE J. Sel. Topics Quantum Electron.*, vol. 2, no. 2, pp. 236–250, Jun 1996.
[43] J. Park, G. Kim, H. Park, J. Joo, S. Kim, and M. J. Kwack, "Performance improvement in silicon arrayed waveguide grating by suppression of scattering near the boundary of a star coupler," *Appl. Opt.*, vol. 54, no. 17, pp. 5597–5602, 2015.